Period doubling and quadrupling of wrinkles in film/substrate bilayers: a nonlinear symplectic analysis

Teng Zhang[a,b,*]

[a] *Department of Mechanical and Aerospace Engineering, Syracuse University, 214 Link Hall, Syracuse, NY, 13244, USA*
[b] *BioInspired Institute, Syracuse University, Syracuse, NY, 13244, USA*

Abstract

Under compression, a stiff film bonded to a soft substrate can progress from sinusoidal wrinkling to period doubling and quadrupling before localization. We develop an analytical-depth Rayleigh–Ritz method for this finite-amplitude cascade. Hamiltonian–Stroh modes represent the homogeneous depth response, nonlinear product rates enrich the finite state, and signed Floquet spaces test secondary stability through the constitutive second variation. For $\mu_f/\mu_s = 100$, the method gives a period-doubling threshold $T_{24} = 0.179$ and a retained-space period-four neutral point $T_{45} = 0.244$. A fixed-grid lattice calculation gives corresponding neutral crossings at 0.176 and 0.243 and produces similar period-two and period-four patterns. The two transitions arise through repeated subharmonic coupling: the primary wrinkle couples the signed half-wavenumber pair, and the doubled state couples the quarter-wavenumber pair. Across modulus ratios from 14 to 375, the primary onset strain varies nearly ninefold, whereas the doubling boundary remains near 0.18. Published incompressible finite-element calculations show the same weak dependence of the secondary boundary on stiffness contrast. The method therefore follows two successive wavelength multiplications without substrate-depth nodal unknowns.

Keywords: wrinkles, period doubling, symplectic elasticity, secondary bifurcation, film/substrate bilayer, post-buckling

---

*Corresponding author. Tel.: +1 315 443 2969.
Email address: tzhang48@syr.edu (Teng Zhang)

1. Introduction

Compressing a stiff thin film bonded to a compliant substrate produces a family of surface instabilities whose richness has made the bilayer a canonical system of nonlinear elasticity, with applications ranging from micropatterning and stretchable electronics to thin-film metrology and the morphogenesis of layered tissues (Bowden et al., 1998; Cerda and Mahadevan, 2003; Li et al., 2012; Holland et al., 2017; Liu and Liu, 2026). The primary instability is sinusoidal wrinkling, and its onset strain and wavelength follow from classical linear analyses. The subsequent evolution is a finite-amplitude problem. As compression increases, the wrinkle may double its period, then quadruple it, and eventually form localized folds or creases (Li et al., 2012; Brau et al., 2013). Experiments have observed period doubling near a compressive strain of 0.2 (Brau et al., 2011), followed at larger strains by folding (Sun et al., 2012). Finite-element phase diagrams organize doubling, quadrupling, creasing and folding as connected stages of the same ruga cascade (Cao and Hutchinson, 2012a; Zhao et al., 2015a); following that diagram's region labels, we write T_{24} for the wrinkle-to-doubled boundary and T_{45} for the doubled-to-quadrupled boundary.

Brau et al. (2011) identified the physical origin of period doubling. A finite wrinkle modulates the stiffness felt by a subharmonic perturbation, producing the resonance structure of a Mathieu oscillator, with substrate nonlinearity breaking the up–down symmetry of the pattern. Numerical continuation has traced the secondary bifurcations and the developed period-doubled states (Xu et al., 2015). Simulations in compression and in growth-driven bilayers show that doubling can be followed by further wavelength multiplication or localization, depending on load and modulus ratio (Sun et al., 2012; Budday et al., 2015; Shen et al., 2024; Zhao et al., 2015a). Ridge localization, creasing and cyclic path dependence provide the wider context for the smooth cascade considered here (Zang et al., 2012; Cao and Hutchinson, 2012b; Diab et al., 2013; Zhao et al., 2016). Compared with period doubling, quadrupling has received less theoretical treatment, in part because its base state is already the finite-amplitude doubled pattern.

The difficulty is that the relevant states are already far from the linear onset of wrinkling. Reduced foundation models capture the resonance picture while necessarily simplifying the substrate response. As Fu and Cai (2015) noted, the equations of the foundation model of Brau et al. (2011) imply that period doubling disappears in the incompressible-substrate limit; this sensitivity to the substrate description motivates treating the substrate with full finite-strain elasticity. Approximate continuum theories followed (Zhao et al., 2015b; Zhuo and Zhang, 2015); Liu and Bertoldi (2015) formulated the stability problem in a general Bloch-wave setting, and related analyses have considered substrate pre-stretch and sandwich systems (Auguste et al., 2014; Guo and Nie, 2024). The asymptotic analyses of Fu and Cai (2015) and Cai and Fu (2019) are the closest continuum theories to the present problem. They use exact nonlinear elasticity, construct the wrinkled state as a weakly nonlinear expansion, and determine the secondary threshold from a solvability condition, the spatial analogue of the parametric-resonance tongue. The two asymptotic formulations give different stiff-film estimates: about 0.228 in the incompressible formulation of Fu and Cai (2015) and about 0.167 in the later compressible formulation of Cai and Fu (2019). Experiments and finite-element simulations commonly report values near 0.19 to 0.20 (Brau et al., 2011; Cao and Hutchinson, 2012a). Because the analytical values come from distinct weakly nonlinear formulations as well as different treatments of compressibility, we use them as historical reference calculations rather than as bounds on the present model. Related asymptotic and numerical work has also traced several successive period-multiplied morphologies (Fu et al., 2022).

Here we ask whether a stationary finite-amplitude wrinkle predicts the observed period-doubling threshold and whether the same subharmonic mechanism persists on the doubled parent to generate period quadrupling. We compute T_{24} from the second variation about a finite Ritz state and compare it with asymptotic theory and a separate lattice calculation. We then use the stationary doubled state as the parent for T_{45}. We also compute developed post-critical doubled states and compare their extrapolated branch intercept with the neutral threshold. The principal objective is to follow successive members of the smooth period-multiplication cascade at finite amplitude.

Our starting point is the symplectic wrinkle formulation. After a Fourier decomposition, incremental equilibrium becomes a Hamiltonian system in the depth coordinate, with displacement and traction as conjugate variables. This state-space framework and its symplectic orthogonality have been used for layered elasticity, wave propagation, two-point boundary-value problems, buckling and singular fields (Zhong and Williams, 1993; Zhong, 1995; Yao et al., 2009; Gao et al., 2004; Peng et al., 2012; Xu et al., 2006; Wang et al., 2016; Zhang and Zhong, 2003). We established the formulation for onset wrinkles in layered neo-Hookean structures (Zhang, 2017) and extended it to layers with graded stiffness (Sui et al., 2019). Those analyses determine the critical strain, wavelength and eigenfunctions.

The weakly nonlinear hierarchy identifies the relevant carriers, reflection sectors and nonlinear product rates. The finite states themselves are stationary points of the unexpanded elastic energy in a Ritz space built from exact Hamiltonian–Stroh modes and analytical product-rate functions. Their stability follows from the constitutive second variation in signed Floquet spaces. A fixed-grid, finite-element-derived lattice model provides an additional comparison of thresholds and morphologies (Zhang, 2019), while a Schur reduction relates the finite Hessian to the classical solvability condition (Fu and Cai, 2015; Cai and Fu, 2019).

The paper is organized as follows. Section 2 formulates the bilayer and recalls the linear symplectic system. Section 3 presents the weakly nonlinear analysis. Section 4 constructs the finite-amplitude analytical-depth energy method. Section 5 applies it to period doubling, and Section 6 applies the same framework about the doubled state to period quadrupling. Section 7 examines the doubling boundary across the modulus ratio. Section 8 discusses what the Hamiltonian structure provides, and Section 9 concludes.

2. Problem formulation

We consider plane strain compression of a bilayer: a film of thickness h and shear modulus μ_f bonded to a deep substrate of shear modulus μ_s, with modulus ratio $\mu_f/\mu_s = 100$ unless stated otherwise. Both layers are compressible neo-Hookean solids with strain energy density

$$W = \frac{\mu}{2}\left(I_1 - 2\right) - \mu \ln J + \frac{\kappa}{2}\left(J - 1\right)^2, \tag{1}$$

where $I_1 = \mathbf{F}:\mathbf{F}$ in plane strain, $J = \det \mathbf{F}$, and κ is the first Lamé parameter in the small-strain limit, so that $\nu = \kappa/(2(\kappa + \mu)) \approx 0.476$ for the ratio $\kappa/\mu = 20$ used in both layers; the shared ratio also gives the two layers a common transverse stretch in the homogeneous state. The μ terms of Eq. (1) are those of our linear analysis (Zhang, 2017). In plane strain, Eq. (1) coincides with the compressible neo-Hookean limit used by Cai and Fu (2019), with their volumetric coefficient identified as κ. Their calculation at $\mu_f/\mu_s = 100$ therefore provides a benchmark with the same strain-energy form and stiffness ratio. The approximations remain different: Cai and Fu use a weakly nonlinear solvability expansion, whereas the present calculation uses a finite Ritz state and the unexpanded constitutive second variation.

The first Piola stress of Eq. (1) is

$$\mathbf{P} = \frac{\partial W}{\partial \mathbf{F}} = \mu\,\mathbf{F} + \left(\kappa\,(J-1) - \frac{\mu}{J}\right)\operatorname{cof}\mathbf{F}, \qquad \operatorname{cof}\mathbf{F} = J\mathbf{F}^{-T}. \tag{2}$$

The bilayer is compressed by a nominal strain $\delta = 1 - \lambda_1$, applied as a uniform stretch λ_1 along X_1; the transverse stretch λ_2 of each layer follows from the traction-free condition $P_{22}(\lambda_1, \lambda_2) = 0$ of the homogeneous state $\mathbf{F}_0 = \operatorname{diag}(\lambda_1, \lambda_2)$. Displacements are measured from this homogeneous state,

$$x_1 = \lambda_1 X_1 + u_1, \qquad x_2 = \lambda_2 X_2 + u_2. \tag{3}$$

For a perturbation of wavenumber k, $u_i = e^{ikX_1} U_i(X_2)$, the energy expanded to second order in $\mathbf{u}$ becomes, per unit length of X_1,

$$\mathcal{E}_2 = \frac{1}{2}\int \Big[\mathbf{U}'^{\mathrm{H}}\mathbf{K}_{22}\,\mathbf{U}' + \mathbf{U}'^{\mathrm{H}}\mathbf{K}_{21}\,\mathbf{U} + \mathbf{U}^{\mathrm{H}}\mathbf{K}_{21}^{\mathrm{H}}\,\mathbf{U}' + \mathbf{U}^{\mathrm{H}}\mathbf{K}_{11}\,\mathbf{U}\Big]\mathrm{d}X_2, \tag{4}$$

where the prime denotes $\mathrm{d}/\mathrm{d}X_2$, superscript $^{\mathrm{H}}$ denotes conjugate transpose, and the two-by-two matrices

$$(\mathbf{K}_{22})_{ij} = \mathcal{A}^0_{i2j2}, \qquad (\mathbf{K}_{21})_{ij} = ik\,\mathcal{A}^0_{i2j1}, \qquad (\mathbf{K}_{11})_{ij} = k^2\mathcal{A}^0_{i1j1} \tag{5}$$

collect the incremental moduli $\mathcal{A}^0 = \partial^2 W/\partial\mathbf{F}\,\partial\mathbf{F}$ evaluated at $\mathbf{F}_0$. Following Zhang (2017) we define

$$\mathbf{p} = -\Big(\mathbf{K}_{22}\,\mathbf{U}' + \mathbf{K}_{21}\,\mathbf{U}\Big), \tag{6}$$

minus the linearized traction amplitude on planes of constant X_2; with this definition, eliminating $\mathbf{U}'$ in favor of $\mathbf{p}$ converts the Euler–Lagrange equations of (4) into the Hamiltonian system

$$\mathbf{V}' = \mathbf{H}(k, \lambda_1)\,\mathbf{V}, \qquad \mathbf{V} = \begin{pmatrix}\mathbf{q}\\ \mathbf{p}\end{pmatrix}, \qquad \mathbf{H} = \begin{bmatrix}\mathbf{A} & \mathbf{D}\\ \mathbf{B} & -\mathbf{A}^{\mathrm{H}}\end{bmatrix}, \tag{7}$$

with $\mathbf{q} = \mathbf{U}$ and

$$\mathbf{A} = -\mathbf{K}_{22}^{-1}\mathbf{K}_{21}, \qquad \mathbf{B} = -\Big(\mathbf{K}_{11} - \mathbf{K}_{21}^{\mathrm{H}}\mathbf{K}_{22}^{-1}\mathbf{K}_{21}\Big), \qquad \mathbf{D} = -\mathbf{K}_{22}^{-1}. \tag{8}$$

Zhang (2017) derived this construction and showed that it satisfies the adjoint symplectic identity

$$\mathbf{H}^{\mathrm{H}}\mathbf{J}_s + \mathbf{J}_s\mathbf{H} = \mathbf{0}, \qquad \mathbf{J}_s = \begin{bmatrix}\mathbf{0} & \mathbf{I}\\ -\mathbf{I} & \mathbf{0}\end{bmatrix}; \tag{9}$$

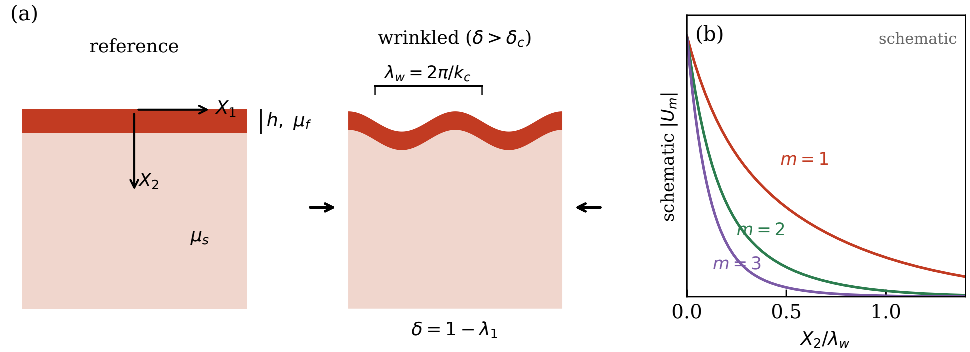

Figure 1: (a) Reference and wrinkled configurations of the bilayer. A film of thickness h and modulus μ_f on a deep substrate of modulus μ_s is compressed by a nominal strain $\delta = 1 - \lambda_1$; wrinkles of wavelength $\lambda_w = 2\pi/k_c$ appear beyond δ_c. Following our linear analyses, X_2 points from the film surface into the depth. (b) Schematic depth profiles illustrating the analytical representation. Exact homogeneous Hamiltonian–Stroh modes are supplemented by analytical product-rate Ritz functions, giving a global analytical-depth span for each harmonic.

only the moduli $\mathcal{A}^0$ differ here, through the volumetric term of Eq. (1). Onset wrinkling is the linear eigenvalue problem of Eq. (7): a traction-free surface, $\mathbf{p} = 0$ at $X_2 = 0$, continuity of $\mathbf{V}$ at the interface, and decay in the deep substrate admit a nontrivial solution first at $\delta_c = 0.0239$, with wavenumber $k_c h = 0.299$, consistent with the stiff-film estimate $(3\mu_s/\mu_f)^{1/3}$.

Two properties of Eq. (7) carry the nonlinear development below. Its eigenpairs supply the exact homogeneous exponential depth profiles at each wavenumber: four rates in the film and the two-dimensional decaying invariant subspace in the deep substrate. Products of such fields generate additional, composite rates. In the finite-amplitude calculation those product rates organize kinematically admissible Ritz enrichments; they are not asserted to be further eigenmodes of $\mathbf{H}$. Figure 1 sketches the geometry and this structure.

3. Weakly nonlinear symplectic analysis

3.1. The weakly nonlinear wrinkled state

We first construct the classical weakly nonlinear post-buckling expansion within the symplectic framework. The wrinkled state is expanded about the critical point in powers of an amplitude ε,

$$\mathbf{u} = \varepsilon\,\mathbf{u}^{(1)} + \varepsilon^2\mathbf{u}^{(2)} + \varepsilon^3\mathbf{u}^{(3)} + \cdots, \qquad \mathbf{u}^{(1)} = \mathrm{Re}\Big[\mathbf{U}_1^c(X_2)\,e^{ik_cX_1}\Big], \tag{10}$$

where $\mathbf{U}_1^c$ is the onset eigenfunction of Section 2, normalized to unit vertical surface displacement, so that ε is the surface amplitude of the fundamental. Because the wrinkle is a material pattern, its reference wavenumber remains the critical k_c selected at onset, so all harmonics here and below are taken in the reference coordinate X_1, and the current wavelength is $\lambda_1\lambda_w$ with $\lambda_w = 2\pi/k_c$. Expanding the energy density about the homogeneous state,

$$W = W_0 + \mathbf{P}_0 : \nabla\mathbf{u} + \tfrac{1}{2}\,\mathcal{A}^0 : \nabla\mathbf{u} : \nabla\mathbf{u} + \tfrac{1}{3!}\,\mathcal{A}^1 \therefore (\nabla\mathbf{u})^3 + \tfrac{1}{4!}\,\mathcal{A}^2 :: (\nabla\mathbf{u})^4 + \cdots, \tag{11}$$

where $\mathcal{A}^n = \partial^{n+2}W/\partial\mathbf{F}^{n+2}\Big|_{\mathbf{F}_0}$ and $\mathbf{P}_0 = \partial W/\partial\mathbf{F}|_{\mathbf{F}_0}$. The periodic-cell integral of the linear term vanishes under the homogeneous traction and periodicity conditions: $P^0_{22} = 0$, the base shear tractions vanish, and the integral of $u_{1,1}$ is zero. The remaining terms define the linear, quadratic and cubic parts of the equilibrium operator, $\mathcal{L}\mathbf{u} = -\mathrm{Div}(\mathcal{A}^0 : \nabla\mathbf{u})$, $\mathcal{Q}(\mathbf{u},\mathbf{u}) = -\frac{1}{2}\mathrm{Div}(\mathcal{A}^1 : \nabla\mathbf{u}\nabla\mathbf{u})$, and $\mathcal{C}(\mathbf{u},\mathbf{u},\mathbf{u}) = -\frac{1}{6}\mathrm{Div}(\mathcal{A}^2 \therefore (\nabla\mathbf{u})^3)$; the traction-free surface and the interface conditions expand in the same way and supply the boundary terms at each order. Because the critical point is where $\mathcal{L}$ first acquires the onset eigenfunction in its kernel, the load must be expanded with the state, $\delta = \delta_c + \varepsilon^2\delta_2 + \cdots$, so that $\mathcal{L} = \mathcal{L}_c + \varepsilon^2\delta_2\,\partial_\delta\mathcal{L}|_c + \cdots$, and the hierarchy reads

$$\begin{aligned}
\mathcal{L}_c\,\mathbf{u}^{(2)} &= -\mathcal{Q}\Big(\mathbf{u}^{(1)},\mathbf{u}^{(1)}\Big),\\
\mathcal{L}_c\,\mathbf{u}^{(3)} &= -\delta_2\,\partial_\delta\mathcal{L}|_c\,\mathbf{u}^{(1)} - 2\,\mathcal{Q}\Big(\mathbf{u}^{(1)},\mathbf{u}^{(2)}\Big) - \mathcal{C}\Big(\mathbf{u}^{(1)},\mathbf{u}^{(1)},\mathbf{u}^{(1)}\Big),
\end{aligned} \tag{12}$$

and so on. The quadratic forcing appears in the mean field and second harmonic, so $\mathbf{u}^{(2)}$ carries wavenumbers 0 and $2k_c$; its depth profiles are particular exponentials whose rates are pairwise sums of the rates of $\mathbf{U}_1^c$ (for the mean field, sums of a rate and a conjugate rate), completed by homogeneous modes of $\mathbf{H}(0,\lambda_1)$ and $\mathbf{H}(2k_c,\lambda_1)$ that restore the surface and interface conditions. The first equation is solvable because its forcing lives away from the critical wavenumber. The second has forcing at k_c against the singular operator $\mathcal{L}_c$. Orthogonality of its right-hand side to the onset eigenfunction gives the solvability condition that determines δ_2 and hence the local primary-amplitude relation $\varepsilon^2 = (\delta-\delta_c)/\delta_2$; the sign of δ_2 fixes the local branch direction. The displayed hierarchy supplies the carrier, symmetry and product-rate organization used below. No higher-order weak coefficients are reported or used in the present calculation.

3.2. Subharmonic stability criterion

Period doubling is a question of linear stability of the state (10) against subharmonic perturbations. The criterion depends on the wrinkled state, rather than on the method used to obtain it, and is applied in Section 4 to a finite-amplitude Ritz state. The second variation of the energy about a wrinkled state $\mathbf{u}_w$ is

$$\delta^2\Pi[\mathbf{v}] = \frac{1}{L}\int_0^L\int_0^\infty \nabla\mathbf{v} : \mathcal{A}(X_1, X_2) : \nabla\mathbf{v}\,\mathrm{d}X_2\,\mathrm{d}X_1, \qquad \mathcal{A} = \left.\frac{\partial^2 W}{\partial\mathbf{F}\,\partial\mathbf{F}}\right|_{\mathbf{F}_0+\nabla\mathbf{u}_w}, \tag{13}$$

and the tangent moduli $\mathcal{A}$ inherit the wrinkle's periodicity,

$$\mathcal{A}(X_1, X_2) = \sum_m \hat{\mathcal{A}}_m(X_2)\,e^{imk_cX_1}, \qquad \hat{\mathcal{A}}_{-m} = \overline{\hat{\mathcal{A}}_m}. \tag{14}$$

A Bloch perturbation at half the wrinkle wavenumber therefore couples an entire comb of modes,

$$\mathbf{v} = \sum_{n=-N}^{N-1} \mathbf{v}_n(X_2)\,e^{i(n+1/2)k_cX_1}, \qquad \mathbf{v}_{-n-1} = \overline{\mathbf{v}_n}, \tag{15}$$

with signed wavenumbers $\{\dots, -\frac{3}{2}, -\frac{1}{2}, +\frac{1}{2}, +\frac{3}{2}, \dots\}k_c$: the component $\hat{\mathcal{A}}_m$ scatters $\mathbf{v}_n$ into $\mathbf{v}_{n\pm m}$. Restricted to the comb, Eq. (13) defines a stiffness operator whose softest generalized eigenvalue $\chi_0(\delta)$ measures the stability of the wrinkle against period doubling; the threshold is the zero crossing,

$$\chi_0(\delta^*) = 0. \tag{16}$$

At its leading truncation the signed pair $\pm k_c/2$ is retained. The fundamental component $\hat{\mathcal{A}}_1$ couples the two members directly: a mode at $+k_c/2$ is scattered to $-k_c/2$ (and conversely) by the modulation at k_c. This is the parametric resonance structure of a Mathieu problem, with $\hat{\mathcal{A}}_1$ as the drive; the picture goes back to Brau et al. (2011), and the same coupling underlies the solvability analysis of Fu and Cai (2015). Reflection about a crest or valley separates this real Floquet space into two sectors, and the physical period-doubling mode is followed by continuation. In the implementation, each positive carrier label expands into real cosine and sine columns and therefore represents the full conjugate pair $\pm m$ in Eq. (15).

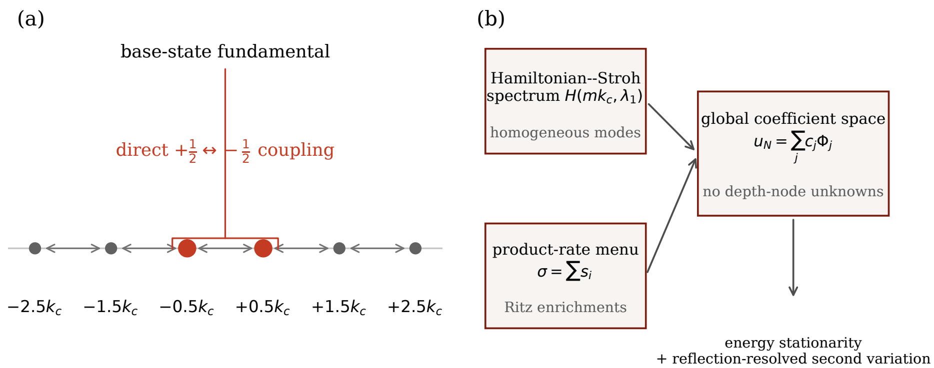

Figure 2: Signed Floquet and analytical-depth constructions used in the finite-amplitude calculation. (a) The signed half-harmonic Floquet comb; the base-state fundamental couples $+k_c/2$ directly to $-k_c/2$. (b) Exact homogeneous Hamiltonian–Stroh modes and product-rate Ritz enrichments form the analytical-depth trial space; a blockwise Gram selection (not shown) then filters the redundant dictionary. Energy stationarity determines the finite state, and the reflection-resolved second variation determines stability.

3.3. Scope of the weakly nonlinear analysis

The weak hierarchy identifies the carrier, symmetry, and product-rate structure. At each order, the known forcing defines an inhomogeneous depth problem whose solution combines homogeneous Hamiltonian modes with particular profiles at product rates, as in the asymptotic literature. Solvability at the singular fundamental block determines the local primary-amplitude relation, but it does not determine the finite amplitude of a secondary state far from primary onset.

For the parameters considered here, the secondary instability lies outside the small-amplitude neighborhood of primary onset, so truncation of the parent state can materially affect its second variation. Accordingly, the weak hierarchy is used here to construct the carriers, signed Floquet sectors and product-rate menus of Section 4 (Figure 2). The reported T_{24} and T_{45} values come from the finite-amplitude energy calculation; the published asymptotic values of Fu and Cai (2015) and Cai and Fu (2019) serve as comparisons.

4. Symplectic-basis Rayleigh–Ritz method

4.1. Analytical representation of the finite-amplitude state

The buckled displacement field is expanded in Fourier harmonics of the wrinkle wavenumber,

$$\mathbf{u}_N(X_1, X_2) = \mathrm{Re}\sum_{m=0}^{N} \mathbf{U}_m(X_2)\, e^{imk_c X_1}. \tag{17}$$

The depth profiles $\mathbf{U}_m$ are not discretized on a mesh; the unknowns are global coefficients. In each layer, the eigenmodes of $\mathbf{H}(mk_c, \lambda_1)$, linearized about the flat state at the current load, provide exact homogeneous trial components for harmonic m, while products of lower harmonics, organized by the weakly nonlinear hierarchy of Section 3, suggest additional composite rates. The Hamiltonian structure therefore supplies the homogeneous backbone and organizes a compact trial dictionary. Each profile is expanded as

$$\mathbf{U}_m(X_2) = \sum_a c_{ma}\, \boldsymbol{\varphi}_{ma}(X_2) \tag{18}$$

with two families of analytic functions $\boldsymbol{\varphi}_{ma}$. The homogeneous family combines the eigenpairs $(s_i, \mathbf{v}_i)$, $\mathbf{v}_i = (\mathbf{q}_i, \mathbf{p}_i)^\mathsf{T}$, of $\mathbf{H}(mk_c, \lambda_1)$ in the film with the decaying pairs $(t_j, \mathbf{w}_j)$, $\mathbf{w}_j = (\mathbf{r}_j, \boldsymbol{\tau}_j)^\mathsf{T}$, in the substrate,

$$\boldsymbol{\varphi}(X_2) = \begin{cases} \displaystyle\sum_{i=1}^{4} a_i\, \mathbf{q}_i\, e^{s_i X_2}, & 0 \le X_2 \le h, \\ \displaystyle\sum_{j=1}^{2} b_j\, \mathbf{r}_j\, e^{t_j (X_2 - h)}, & X_2 \ge h, \end{cases} \tag{19}$$

with the six coefficients restricted by continuity of displacement and traction at the interface, four conditions whose null space yields two admissible modes per harmonic. The enrichment family consists of componentwise exponentials at product rates assembled from the relevant parent-carrier film and substrate rate pools. Products of exponential depth profiles add their rates, while horizontal-wavenumber selection determines which harmonic an interaction can drive. The weak hierarchy therefore supplies candidate composite rates for each harmonic,

$$\sigma \in \bigcup_{p \in \mathcal{P}_m} \Big\{ s_{i_1} + s_{i_2} + \cdots + s_{i_p} \Big\}, \tag{20}$$

where the finite menu $\mathcal{P}_m$ retains a tractable set of low-order interactions suggested by that hierarchy. Nested calculations enlarge the menu by adding the next product order of the same parity; the exact production menus are listed in Appendix A. Doubled-cell dictionaries—including the even-only period-one calculation—use the union of the k_c and $k_c/2$ carrier rates. Film and substrate pools are formed separately; a film exponential is continued into the substrate by the two decaying modes of $\mathbf{H}(mk_c, \lambda_1)$ with amplitudes fixed by displacement continuity at the interface. These displacement-continuous functions serve as kinematically admissible Ritz enrichments; energy stationarity determines their collective weights. Rate sums are generated separately in the film and substrate, deduplicated and screened. The units, cutoffs, order menus and final settings are given in Table A.1. Surface traction balance and interface traction continuity enter the variational equations naturally rather than being imposed on every enrichment function.

The mean harmonic requires separate treatment. At $m = 0$ the ordinary nonzero-wavenumber Stroh construction is degenerate. Rigid translation is removed. Crest-centered reflection symmetry excludes an X_1-independent horizontal displacement, so only the vertical mean correction is represented with even product-rate functions; the imposed uniform stretches already reside in $\mathbf{F}_0$.

Within each harmonic block, we form the gradient-seminorm Gram matrix, diagonalize it, and retain eigendirections whose eigenvalues exceed a relative cutoff times the largest eigenvalue of that block. The cutoff is tightened as a refinement variable, and the retained rank is reported. This is the spectral-truncation principle used to regularize approximation in redundant frames (Adcock and Huybrechs, 2019). This blockwise orthonormalization controls the severe redundancy of the analytical dictionary without introducing depth-nodal degrees of freedom. Thousands of candidate functions are reduced to a few hundred global coordinates; the final ranks are listed in Table A.1.

The nonlinear unknowns are the retained analytical displacement coefficients. They are determined from the unexpanded constitutive energy, with no amplitude series. Collecting them in $\mathbf{c}$, the trial state defines the flat-subtracted potential

$$\Pi_N(\mathbf{c}; \delta) = \frac{1}{L} \int_0^L \int_0^\infty \left[W\Big(\mathbf{F}_0 + \nabla \mathbf{u}_N(\mathbf{c})\Big) - W(\mathbf{F}_0) \right] \mathrm{d}X_2 \, \mathrm{d}X_1, \tag{21}$$

evaluated by stated Fourier/Gauss quadrature over the represented cell and a deep analytical tail cutoff. The $\log J$ term and the reciprocal factors in the stress and tangent make the energy, gradient and Hessian quadratures non-polynomial and therefore not algebraically exact. Here L is the reference length of that cell, so the reported energy is a period average per unit reference length. Writing $\boldsymbol{\phi}_a = \partial \mathbf{u}_N / \partial c_a$ for a free retained trial direction, the coefficient equations are

$$0 = \frac{\partial \Pi_N}{\partial c_a} = \frac{1}{L} \int_{\text{cell}} \mathbf{P}\Big(\mathbf{F}_0 + \nabla \mathbf{u}_N\Big) : \nabla \boldsymbol{\phi}_a \, \mathrm{d}V, \qquad a = 1, \ldots, n_N, \tag{22}$$

reached by a damped Newton iteration with the consistent coefficient Hessian $\partial^2 \Pi_N / \partial \mathbf{c}\, \partial \mathbf{c}$. Harmonic and neutral modes initialize the states, which are carried between spaces by physical-field projection and continuation. The translational phase is pinned. Equation (22) enforces continuum virtual work within the retained span; continuation follows a local stationary branch. It does not impose pointwise $\operatorname{Div} \mathbf{P} = \mathbf{0}$ or traction balance as discrete equations; these quantities are evaluated separately to measure unresolved continuum content. Retained-space stability is tested below.

4.2. Stability criterion

Period doubling is detected as in Section 3, by the constitutive second variation (13) projected onto the signed subharmonic comb (15), now evaluated about the stationary Ritz state. Because the tangent moduli are λ_w periodic, the second variation is block diagonal in the Floquet exponent, so the subharmonic comb decouples exactly from perturbations with the wrinkle's own periodicity, and the generalized eigenvalue problem

$$\begin{aligned} &\Big(\mathbf{K}_{\text{comb}} - \chi\, \mathbf{M}\Big)\, \mathbf{w} = \mathbf{0}, \\ &\qquad (\mathbf{K}_{\text{comb}})_{ab} = \frac{1}{L} \int_{\text{cell}} \nabla \boldsymbol{\varphi}_a : \mathcal{A} : \nabla \boldsymbol{\varphi}_b \, \mathrm{d}V, \\ &\qquad M_{ab} = \frac{1}{L} \int_{\text{cell}} \boldsymbol{\varphi}_a \cdot \boldsymbol{\varphi}_b \, \mathrm{d}V. \end{aligned} \tag{23}$$

uses the unexpanded constitutive tangent at the finite state, and the threshold is the zero crossing (16) of its softest eigenvalue χ_0. Here $\boldsymbol{\varphi}_a$ are comb perturbation functions, distinct in general from the finite-state basis, and $\mathbf{M}$ is their period-averaged L^2 Gram matrix, so χ measures the second variation per unit L^2 norm of the perturbation; the location of the zero crossing is independent of the choice of any positive definite $\mathbf{M}$. We form both crest-and valley-reflection sectors from the same signed comb, and identify the physical branch by eigenvector continuation rather than by eigenvalue order alone. The Mathieu-type coupling is therefore retained without reducing the calculation to a single scalar coupling coefficient. The remaining approximations are the state harmonic cutoff, the product-rate menu, the Gram cutoff, the comb depth, the substrate integration cutoff and the quadrature. Their tested refinements and the open refinement directions for T_{45} are documented below and in Appendix A.

4.3. Relation to a solvability reduction

At any fixed retained space, let $\mathbf{K} = \mathbf{K}_{\mathrm{comb}}$ at $\chi = 0$ and partition it into the real span of the signed $\pm k_c/2$ carrier pair and the remaining carriers. Eliminating the remainder gives the Schur complement

$$\mathbf{S} = \mathbf{K}_{hh} - \mathbf{K}_{hr}\,\mathbf{K}_{rr}^{-1}\,\mathbf{K}_{rh}, \qquad \det\mathbf{K} = \det\mathbf{K}_{rr}\,\det\mathbf{S}, \tag{24}$$

provided $\mathbf{K}_{rr}$ is nonsingular. Equation (24) is exact within the retained matrix and exposes the algebraic form of the classical solvability reduction: the eliminated carriers renormalize the half-wavenumber stiffness. The finite daughter amplitude still follows from stationarity of the enlarged nonlinear space. We use this identity as a structural comparison with the Fu–Cai calculation; its numerical check is reported in Appendix A.

4.4. Verification

The energy, stress and tangent implementations are cross-checked by automatic differentiation and regression tests. Retained spaces are assessed through projection, energy and neutral-eigenvalue changes. For the final period-one state at $\delta = 0.18$, the coefficient-gradient norm is below 10^{-9} and the projection residual from the preceding space is below 10^{-4}.

We also evaluate strong-form balance of the stress field obtained from each Ritz state. Each L^2 norm below is evaluated in the reference configuration, with measure $\mathrm{d}X_1\mathrm{d}X_2$, over one period in X_1 and separately over the film or substrate in X_2; the substrate integral uses the $120h$ diagnostic cutoff specified in Appendix A. Within either layer, define

$$R_{\mathrm{str}} = \frac{\|\partial_1\mathbf{P}_{\cdot 1} + \partial_2\mathbf{P}_{\cdot 2}\|_{L^2}}{\left(\|\partial_1\mathbf{P}_{\cdot 1}\|_{L^2}^2 + \|\partial_2\mathbf{P}_{\cdot 2}\|_{L^2}^2\right)^{1/2}}. \tag{25}$$

Its denominator is the root-sum-square size of the two stress-gradient terms that cancel in equilibrium. Surface and interface traction residuals are divided by $S_t = \max\{\mu_f \max_{X_1} \|\nabla\mathbf{u}(X_1, 0)\|_F, \mu_s\}$, the characteristic incremental stress used in the numerical diagnostics. The final period-one state has $R_{\mathrm{str}} < 10^{-2}$ in both layers and surface and interface traction residuals below 10^{-4}. Exact values are given in Appendix A.

For a separate comparison, we also use the real-space lattice construction derived from finite elements by Zhang (2019) for the same energy. Quadrilateral cells carry stretch springs of stiffness

$$k_{ab} = -\mu_e \int_{\Omega_e} \nabla N_a \cdot \nabla N_b \, \mathrm{d}A, \tag{26}$$

where μ_e is the shear modulus assigned to cell e. These springs reproduce the $\mu(I_1 - 2)/2$ term of Eq. (1) exactly for bilinear shape functions N_a, while the remaining terms of Eq. (1) act on the mean dilatation $\bar{J}_e$ of each cell. This fixed-grid lattice provides a separate spatial discretization of the same constitutive model. Neutral thresholds are obtained from eigenvalue sign-change brackets about tightly relaxed parent states. All reported lattice calculations use four wavelengths ($\lambda_w = 21.05h$), 40 elements per wavelength ($\Delta X_1 = 0.526h$), eight elements through the film, and 102 graded elements through a substrate of depth $20\lambda_w$; the mesh contains 17,871 nodes and 17,600 quadrilateral elements. Figure 3 compares a relaxed period-one lattice state with the Ritz state. The lattice daughter states used in Figure 7 must reach an amplitude plateau and pass the looser fixed-grid gradient filter listed in Appendix A; they are used to compare finite-amplitude morphology and amplitude, not to determine a neutral threshold or classify the local bifurcation.

5. Period doubling

The finite wrinkle loses stability in the signed $\pm k_c/2$ sector. Continuation along this neutral direction breaks the equivalence of adjacent wrinkles and produces alternating deep and shallow valleys. We first show the daughter morphology and then determine the neutral crossing.

5.1. The period-doubled state

Figure 4 shows the characteristic geometry at $\delta = 0.24$. In the Ritz calculation, the signed half-wavenumber mode is lifted into a doubled cell

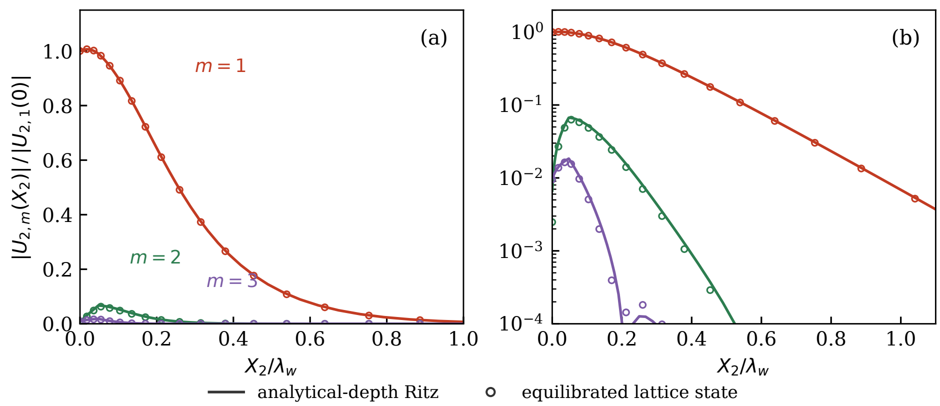

Figure 3: Vertical-displacement depth profiles of the wrinkled state at $\delta = 0.18$: harmonics $|U_{2,m}(X_2)|$ from the Ritz state (lines) and the lattice state (circles), each normalized by its surface fundamental, on (a) linear and (b) logarithmic scales. The smooth lines evaluate the global analytical basis; the lattice symbols provide a depth-profile comparison.

and added to the period-one state; all retained coefficients are then relaxed through energy stationarity. The lattice calculation produces the same alternating pattern.

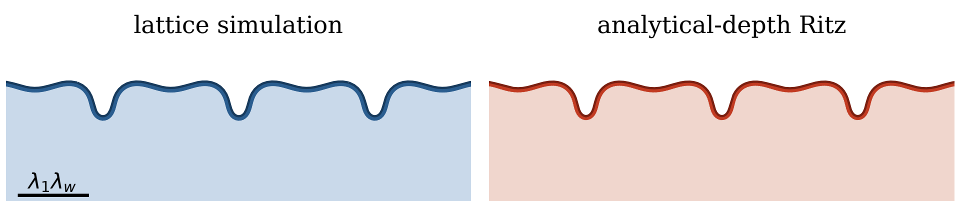

Figure 4: Period-doubled morphology at $\delta = 0.24$. Both the lattice calculation (left) and the symplectic-basis Ritz calculation (right) produce alternating deep and shallow valleys; darker shades are the film and lighter shades the substrate. Both panels use identical coordinate limits normalized by λ_w; the scale bar in the left panel applies to both.

5.2. Finite-amplitude daughter branch

Figure 5 plots the half-wavenumber amplitude together with the neutral thresholds. Let A be the absolute vertical surface Fourier coefficient at $k_c/2$ and $a = A/h$. Over the sampled range $0.19 \le \delta \le 0.22$, the Ritz daughter states follow

$$a^2 = C\,(\delta - \delta_{\text{fit}}), \tag{27}$$

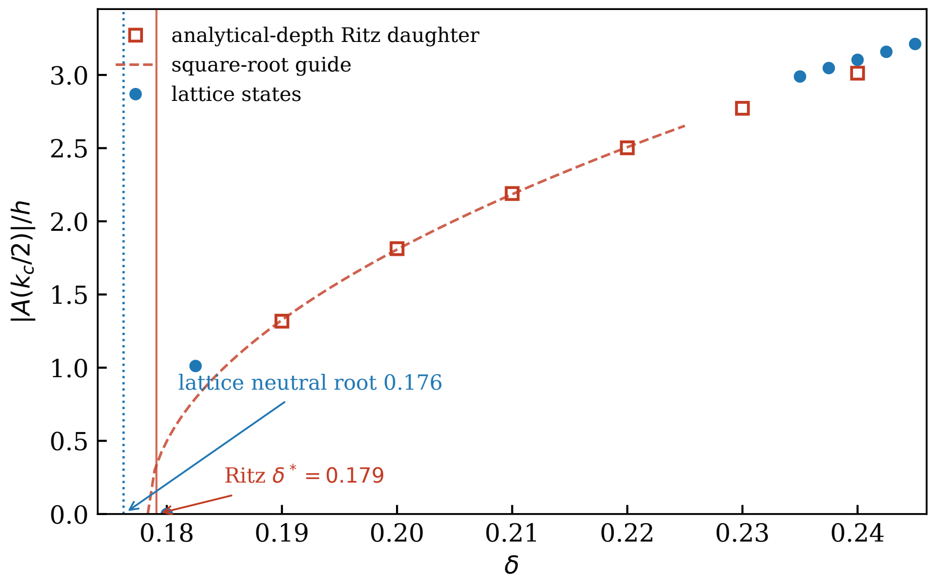

Figure 5: Surface half-wavenumber amplitude $a = |A(k_c/2)|/h$. Red squares are stationary Ritz states, and the dashed curve is the square-root guide fitted over $0.19 \leq \delta \leq 0.22$. Blue points are lattice states satisfying $\|\nabla E\|_2 < 10^{-6}$. Vertical markers show the neutral crossings obtained from the two stability calculations.

with positive C. Its extrapolated intercept is approximately 0.178, close to the separately computed neutral threshold 0.179. This agreement supports interpreting the developed daughter states as the continuation of the half-wavenumber instability. The first sampled daughter already has $a \simeq 1.3$, however, so the fit describes the developed branch rather than its infinitesimal neighborhood; no local normal-form classification is inferred. The lattice states provide a comparison of the branch scale. The fitted coefficients are given in Appendix A.

5.3. Nested threshold estimate

Extending the signed Floquet comb produces the dominant correction to the neutral crossing. Subsequent enrichment of the parent state, product-rate space and Gram cutoff gives progressively smaller changes (Figure 6; the full sequence is given in Table A.2). We therefore report

$$\delta^* = T_{24} = 0.179. \tag{28}$$

For the lattice grid used here, the crossing is 0.176. We do not claim a mesh-extrapolated lattice threshold. Both calculations place the transition near the 0.18–0.20 range reported by experiments and finite-element studies (Brau et al., 2011; Cao and Hutchinson, 2012a; Zhao et al., 2015a).

For comparison, the compressible Cai–Fu formulation gives 0.167 near $\nu \simeq 0.476$ (Cai and Fu, 2019), whereas the earlier incompressible Fu–Cai formulation gives 0.228 (Fu and Cai, 2015). The present value is obtained by a different route: the constitutive second variation about a finite Ritz state.

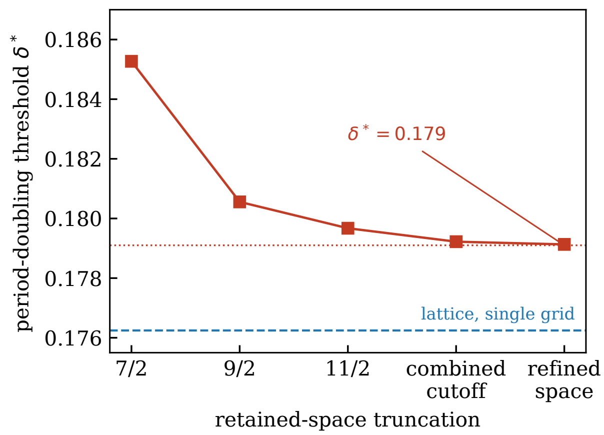

Figure 6: Nested period-doubling calculation. Extending the signed Floquet comb gives the principal correction; subsequent parent-state and product-rate enrichment approach the reported value. The dashed marker is the fixed-grid lattice crossing.

6. Period quadrupling

Period quadrupling repeats the subharmonic mechanism on the doubled parent. Its fundamental wavenumber $q = k_c/2$ couples the signed pair $\pm q/2$, or equivalently $\pm k_c/4$. We therefore test the stationary doubled state in the quarter-wavenumber Floquet comb

$$\{\ldots, -3/4, -1/4, +1/4, +3/4, \ldots\}k_c.$$

To construct a finite period-four state, the doubled parent and its critical quarter-wavenumber mode are lifted into a common $k_c/4$ cell. Product-rate functions associated with the $k_c/4$ and $k_c/2$ carriers enrich this space. The neutral mode seeds continuation, after which all retained coefficients are

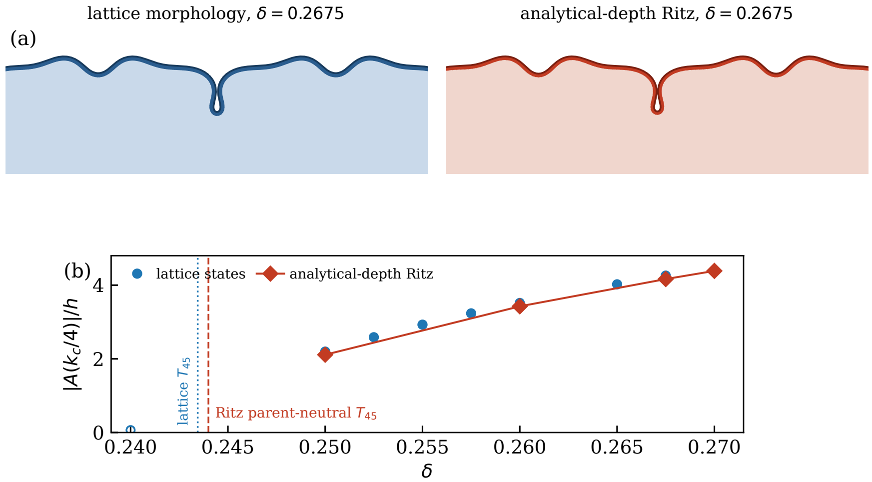

Figure 7: Period quadrupling. (a) Lattice (left) and symplectic-basis Ritz (right) morphologies at $\delta = 0.2675$. (b) Surface quarter-wavenumber amplitude along the lattice and Ritz branches. The red line connects Ritz continuation states; blue symbols show lattice states. The vertical markers show the parent-state neutral crossings. The open lattice symbol at $\delta = 0.24$ is a subthreshold control: its seeded quarter-wavenumber component decays toward the doubled parent rather than developing into the finite-amplitude branch. The two morphology panels use identical coordinate limits normalized by λ_w, each spanning $5.2\lambda_w$ horizontally.

relaxed through energy stationarity. The complementary reflection sector is checked separately.

The quarter-comb eigenvalue changes sign between $\delta = 0.24$ and 0.25. Three coupled refinements of the doubled parent and quarter-wavenumber comb give 0.245792, 0.244645 and 0.244001; the final nested increment is 6.4×10^{-4}. We therefore report the retained-space neutral estimate

$$T_{45} = 0.244. \tag{29}$$

In the reported Ritz spaces, this is the zero of the lowest quarter-comb Hessian eigenvalue: the doubled parent loses quadratic stiffness to a period-four perturbation. The full sequence is reported in Table A.3.

Because the substrate-depth quadrature and the Gram/product-order refinements were not varied independently at the final space, T_{45} is a retained-space estimate.

On the same single grid, the lattice crosses at 0.243. The incompressible finite-element phase diagram places the boundary near 0.26 (Zhao et al., 2015a). The lattice calculation and the finite-element phase diagram both show the wrinkle–double–quadruple sequence and place quadrupling in the same finite-strain range. A same-model continuum calculation would be needed for a quantitative threshold comparison. Across the three coupled rungs at $\delta = 0.24$, the film/substrate R_{str} ratios are 0.276/0.266, 0.233/0.263 and 0.216/0.260: the film ratio decreases monotonically, while the substrate ratio remains near 0.26. This shows improvement in the film but not continuum closure, so the continuum accuracy of T_{45} remains open.

Above the neutral crossing, both calculations develop a period-four morphology (Figure 7). The quarter-wavenumber amplitude grows rapidly over the sampled interval, and the two branches show the same succession of unequal valleys. The lattice amplitudes are slightly larger, and the lattice valleys are sharper, which may reflect smoothing by the finite harmonic Ritz space.

At the displayed load $\delta = 0.2675$, the Ritz state, relaxed without prescribing its quarter-wavenumber amplitude, lies below the lifted doubled parent in energy, is stable modulo translation in both tested reflection sectors and has a positive deformation Jacobian, with no self-intersection detected. It is therefore a stationary period-four morphology of the retained Ritz space. Its strong-form imbalance remains appreciable, particularly in the film, so continuum-level refinement remains open.

7. Dependence of period doubling on the modulus ratio

Primary wrinkling depends strongly on the film/substrate stiffness contrast, whereas published phase diagrams suggest that period doubling is much less sensitive (Zhao et al., 2015a,b). We test this contrast at four modulus ratios using the same reduced Ritz and Floquet refinement protocol. The primary onset, period-one parents and signed half-wavenumber stability problem are recomputed at each ratio; the settings are given in Appendix A. Following the phase-diagram convention, we write $\bar{k} = (3\mu_s/\mu_f)^{1/3}$.

The sweep reveals a clear separation of sensitivities. As μ_f/μ_s decreases from 375 to 14, the primary wrinkling strain rises from 0.010 to 0.087, nearly a ninefold change, whereas T_{24} remains close to 0.18. The stiffness contrast therefore governs primary onset much more strongly than the secondary loss of stability of the developed wrinkle.

Nonlinear finite-element calculations likewise find weak modulus dependence of period doubling for stiff-film bilayers (Zhao et al., 2015b). The

Table 1: Primary wrinkling strain and period-doubling boundary across film/substrate modulus ratios. Values use the same reduced protocol at every ratio; Appendix A gives additional digits. At $\mu_f/\mu_s = 100$, the deeper retained-space hierarchy gives the headline threshold in Eq. (28). The modulus ratios follow from the unrounded $\bar{k}$ values; both parameter rows are rounded for display.

$\bar{k}$	0.20	0.31	0.45	0.60
μ_f/μ_s	375	100	33	14
onset δ_c	0.010	0.024	0.050	0.087
T_{24}, this work	0.176	0.179	0.180	0.182

broader ruga-phase diagram places its nearly vertical T_{24} boundary close to 0.18 over the range considered here (Zhao et al., 2015a). Those calculations use incompressible neo-Hookean solids whereas the present model has $\kappa/\mu = 20$, so the comparison concerns the separation of sensitivities rather than pointwise numerical agreement.

8. Discussion

The period-doubling boundary is far less sensitive to stiffness contrast than primary wrinkling onset. The stiffness balance between film and substrate strongly shifts the first instability, but once a developed wrinkle exists, the secondary transition is governed by its periodic tangent stiffness and signed subharmonic coupling. This mechanism then repeats: the primary wrinkle couples the $\pm k_c/2$ pair, and the doubled parent couples the $\pm k_c/4$ pair. The period-four calculation thus places the first two wavelength multiplications within one mechanical picture.

The Ritz and lattice results agree on the ordering and approximate strain range of both transitions. The published finite-element ruga-phase diagram shows the same weak modulus sensitivity of period doubling and the same progression to quadrupling. The period-doubling result is stable under the deepest nested refinement performed here. For quadrupling, the two numerical representations agree on the transition scale. The doubled parent's larger L^2 strong-form imbalance leaves the continuum accuracy of T_{45} open; the period-four daughter's imbalance separately limits the continuum interpretation of the developed morphology.

The Hamiltonian depth structure makes the Ritz calculation compact. Exact homogeneous modes describe the homogeneous response in each layer and select the decaying substrate subspace, while product-rate functions represent the nonlinear response. Their global coefficients follow from energy stationarity without substrate-depth nodal degrees of freedom. Symplectic analysis therefore organizes the trial space; the nonlinear amplitudes themselves are selected variationally. Further enrichment can be assessed through changes in energy and stability together with strong-form balance and traction continuity.

9. Conclusion

A symplectic-basis Rayleigh–Ritz method follows the wrinkle cascade through doubling and quadrupling without substrate-depth nodal unknowns. At $\mu_f/\mu_s = 100$, it gives $T_{24} = 0.179$ and a retained-space period-four neutral point $T_{45} = 0.244$. Both arise from signed subharmonic coupling in the $\pm k_c/2$ and $\pm k_c/4$ sectors. Across the modulus sweep, primary onset varies strongly, but T_{24} stays near 0.18 and is stable under the tested refinement. Continuum assessment of T_{45} requires a richer doubled parent and quarter-wavenumber stability space; the period-four branch requires separate refinement.

Appendix A. Numerical details

Numerical settings and higher-precision checks supporting the main text are collected here.

Appendix A.1. Trial spaces and quadrature

Calculations use nondimensional model units in which the substrate shear modulus is $\mu_s = 1$ and the film thickness is $h = 2$. Each depth rate σ is expressed in the corresponding inverse-length unit. No further rescaling by h, k_c or q precedes rounding. Rate sums are formed with replacement and rounded componentwise to six decimal places before set deduplication. Film columns with conjugate-equivalent keys $(\operatorname{Re}\sigma, |\operatorname{Im}\sigma|)$ are then deduplicated at four decimal places, or six decimal places in the mean block; this second step is not applied to the non-mean and comb substrate columns. Forced film rates satisfy $|\operatorname{Re}\sigma| < 1.2$ in the state dictionary and $|\operatorname{Re}\sigma| < 1.8$ in the stability dictionary, while substrate rates satisfy $\operatorname{Re}\sigma < -10^{-6}$.

Table A.1 lists the final settings. Here n denotes a harmonic of $q = k_c/2$. The enriched parent menu is denoted $\mathcal{P}_n^{\mathrm{hi}} = \mathcal{P}_n^0 \cup \{o + 2 : o \in \mathcal{P}_n^0\}$, where $\mathcal{P}_{1,2}^0 = \{1, 3\}$, $\mathcal{P}_{3,5,6,7,9,11,13,15,17}^0 = \{3\}$, $\mathcal{P}_4^0 = \{2, 4\}$ and $\mathcal{P}_{8,10,12,14,16,18}^0 = \{4\}$.

Mean orders $\{2,4\}$ add pairwise and four-rate sums to the vertical $n=0$ correction; mean order $\{2\}$ adds only pairwise sums. A comb of order p contains the exact homogeneous mode at each listed Floquet carrier and forced rates $\sigma_b + \sum_{r=1}^{o} \sigma_{i_r}$ for $o = 1,\ldots,p$. Here σ_b is the homogeneous rate at the listed Floquet carrier, and each σ_{i_r} is drawn from the indicated parent-rate pool. The T_{24} comb draws the summed rates from the k_c pool, whereas the T_{45} comb uses the union of the q and k_c pools. Positive carrier representatives encode the corresponding signed pairs.

Table A.1: Production settings for T_{24} and T_{45}, with $q = k_c/2$.

setting	T_{24}	T_{45}
parent harmonics on the q cell	even $n = 0, 2, \ldots, 18$	all $n = 0, 1, \ldots, 16$
positive stability carriers	$(2j+1)k_c/2$, $j = 0, \ldots, 7$	$(2j+1)q/2$, $j = 0, \ldots, 14$
product-rate setting	$\mathcal{P}_n^{\mathrm{hi}}$; mean $\{2,4\}$; comb orders 1–4	$\mathcal{P}_n^{\mathrm{hi}}$; mean $\{2\}$; comb orders 1–2
forced-film cutoff (inverse-length units)	1.2 (state), 1.8 (comb)	1.2 (state), 1.8 (comb)
state/stability Gram cutoff	$10^{-14}/10^{-14}$	$10^{-10}/10^{-9}$
state/stability retained rank	298/212	365/252
condition number of stability mass matrix near bracket	1.2×10^{5}	9.3×10^{4}
state/stability quadrature	48 angular points; substrate span $120h$; 3 film and 14 substrate panels, 8-point Gauss	48 angular points; substrate span $120h$; 3 film and 14 substrate panels, 8-point Gauss
auxiliary quadrature/depth check	earlier $11k_c/2$, order-2: $48 \to 64$ angular; span $120h \to 160h$ (16 substrate panels)	earlier $n = 12$, $25q/2$: $48 \to 96$ angular

Appendix A.2. Convergence and equilibrium diagnostics

The balance and traction checks use denser grids than the state and stability assemblies in Table A.1. Period-one checks use 256 angular points, 8 film panels and 16 substrate panels, with 12-point Gauss quadrature. The T_{45} parent checks use 128 angular points, 6 film panels and 14 substrate panels with 10-point Gauss quadrature. Period-four checks use the same depth paneling with 192 angular points. All use a substrate cutoff of $120h$.

At $\delta = 0.18$, the 298-coefficient period-one space has a coefficient-gradient norm of 9.5×10^{-10} and a preceding-space projection residual of 7.2×10^{-5}. Its film/substrate R_{str} and surface/interface traction ratios are $7.7\times10^{-3}/5.3\times10^{-3}$ and $8.3\times10^{-5}/6.4\times10^{-5}$, respectively.

Table A.2 gives the nested period-doubling sequence. Rank is the signed Floquet dimension after Gram filtering; the final two rows enrich the parent and comb together.

Table A.2: Nested period-doubling calculations. Additional digits are retained to show the changes under successive enrichment.

largest positive carrier	rate/Gram setting	retained rank	crossing
$7k_c/2$	baseline	68	0.185270
$9k_c/2$	baseline	84	0.180556
$11k_c/2$	baseline	99	0.179672
$11k_c/2$	joint order-3/10^{-12}	137	0.179221
$15k_c/2$	$n = 18$/order-4/10^{-14}	212	0.179131

The full coupled state/comb sequence for period quadrupling is given in Table A.3. At the $n_{\max} = 16$, $29q/2$ rung, the physical-carrier substrate span is evaluated at $|m|q$. Adding retained directions generated at $\max\{|m|, 1\}q$ changes the crossing by 6.2×10^{-5}. At the $n_{\max} = 12$, $25q/2$ refinement level, an auxiliary calculation using the $\max\{|m|, 1\}q$ continuation changed the crossing by 1.6×10^{-7} when both the parent-state and stability quadratures were increased from 48 to 96 angular points. This check was not repeated for the final $n_{\max} = 16$, $29q/2$ space.

Table A.3: Coupled retained-space sequence for T_{45}. The comb edge is the largest positive carrier relative to $q = k_c/2$.

parent $n_{\max}$ / comb edge	state coordinates	comb rank	crossing
12 / $25q/2$	279	224	0.245792
14 / $27q/2$	322	238	0.244645
16 / $29q/2$	365	252	0.244001

Table A.4: Strong-form and traction diagnostics for the doubled parents used to bracket T_{45}. Surface traction and interface jump are normalized by the characteristic incremental stress defined in Section 4.4.

δ	film R_{str}	substrate R_{str}	surface traction	interface jump
0.24	0.216	0.260	0.00366	0.00239
0.25	0.224	0.302	0.00415	0.00256

For period doubling, the single-grid lattice crossing is 0.176244932 in $[0.175, 0.1775]$. For period quadrupling, it is 0.243448459 in $[0.2425, 0.245]$.

The following Schur-complement check uses the reduced period-doubling protocol with carriers through $11k_c/2$; the headline comb extends through $15k_c/2$. In the reduced space, $\mathbf{K}_{rr}$ remains positive with minimum Gram-whitened eigenvalue 1.00409; the maximum log-determinant identity residual is 1.08×10^{-8}, and the reduced and full crossings differ by 1.5×10^{-6}.

Appendix A.3. Daughter branch and modulus sweep

The period-doubled daughter fit in Eq. (27) gives $C = 150.824230$ and $\delta_{\rm fit} = 0.1783481$ in the plotted normalization. Lattice parents used for neutral crossings satisfy $\|\nabla E\|_2 < 10^{-6}$.

For Table 1, every modulus ratio uses period-one parents through harmonic $n = 8$ on the doubled cell, a signed comb through $11k_c/2$, and a final Gram cutoff of 10^{-12} in the crest-centered reflection sector. The matched-protocol onset values are 0.009990, 0.023941, 0.049648 and 0.087157; the corresponding T_{24} values are 0.176250, 0.179482, 0.179847 and 0.182130. At $\mu_f/\mu_s = 100$, deeper refinement changes the matched-protocol crossing from 0.179482 to the headline value 0.179131 in Table A.2.

Appendix A.4. Period-four branch data

Table A.5 gives the reported Ritz branch. At $\delta = 0.2675$, the energy difference from the lifted parent is -0.0448932 in the nondimensional model units defined above, and the coefficient-gradient norm is 1.53×10^{-10}. The lowest same-reflection eigenvalue is 2.34×10^{-4}, and the first non-phase complementary eigenvalue is 1.33×10^{-4}. The surface/interface traction ratios are 0.01377/0.007998. Geometry checks at 128, 256 and 512 angular samples find no self-intersection or surface–interface intersection.

Table A.5: Stationary period-four Ritz branch. Amplitude is $|A(k_c/4)|/h$; "coordinates" counts retained Ritz coefficients.

δ	coordinates	amplitude	film $R_{\rm str}$	substrate $R_{\rm str}$	$J_{\rm min}$
0.2500	681	2.1115	0.344	0.149	0.840
0.2600	682	3.4254	0.450	0.185	0.814
0.2675	685	4.1657	0.495	0.181	0.797
0.2700	686	4.3873	0.511	0.189	0.792

Period-four lattice daughters in Figure 7 satisfy an amplitude plateau and $\|\nabla E\|_2 \leq 2 \times 10^{-3}$ on the fixed grid; their amplitudes span $A/h = 2.1968$–4.2596. These points support only the finite-amplitude morphology and amplitude comparison; the lattice threshold comes separately from the parent-state Hessian crossing.

CRediT authorship contribution statement

Teng Zhang: Conceptualization, Methodology, Software, Validation, Formal analysis, Investigation, Data curation, Visualization, Writing – original draft, Writing – review and editing, Funding acquisition, Project administration.

Funding

This work was supported by the U.S. National Science Foundation (NSF) under Grant CMMI-1847149. The funder had no role in study design, data collection, analysis or interpretation, manuscript preparation, or the decision to submit the article for publication.

Declaration of competing interest

The author declares that he has no known competing financial interests or personal relationships that could have appeared to influence the work reported in this paper.

Acknowledgments

Computational resources were provided through the Advanced Cyberinfrastructure Coordination Ecosystem: Services & Support (ACCESS), including CloudBank (NSF Awards 1925001 and 2505560) and Jetstream2 (NSF Grant 2005506).

Data availability

The code, numerical data, run records and provenance information supporting this work are available in version 1.0.0 of the companion GitHub repository (Zhang, 2026). The release includes a reproduction map linking each figure and table to its generating scripts, source data and numerical outputs.

Declaration of generative AI and AI-assisted technologies in the manuscript preparation process

During preparation of this work, the author used Anthropic Claude, OpenAI ChatGPT and Codex, Google Gemini, Moonshot Kimi, DeepSeek, Alibaba Qwen and Zhipu GLM to assist with literature and theory discussion, code development and testing, cross-checking derivations and numerical results, technical review, and language editing. After using these services, the author reviewed and edited the content as needed, verified the reported results, and takes full responsibility for the content of the publication.

References

Adcock, B., Huybrechs, D., 2019. Frames and Numerical Approximation. SIAM Rev. 61, 443–473. https://doi.org/10.1137/17M1114697.

Auguste, A., Jin, L., Suo, Z., Hayward, R.C., 2014. The Role of Substrate Pre-Stretch in Post-Wrinkling Bifurcations. Soft Matter 10, 6520–6529. https://doi.org/10.1039/C4SM01038H.

Bowden, N., Brittain, S., Evans, A.G., Hutchinson, J.W., Whitesides, G.M., 1998. Spontaneous Formation of Ordered Structures in Thin Films of Metals Supported on an Elastomeric Polymer. Nature 393, 146–149. https://doi.org/10.1038/30193.

Brau, F., Damman, P., Diamant, H., Witten, T.A., 2013. Wrinkle to Fold Transition: Influence of the Substrate Response. Soft Matter 9, 8177–8186. https://doi.org/10.1039/C3SM50655J.

Brau, F., Vandeparre, H., Sabbah, A., Poulard, C., Boudaoud, A., Damman, P., 2011. Multiple-Length-Scale Elastic Instability Mimics Parametric Resonance of Nonlinear Oscillators. Nat. Phys. 7, 56–60. https://doi.org/10.1038/nphys1806.

Budday, S., Kuhl, E., Hutchinson, J.W., 2015. Period-Doubling and Period-Tripling in Growing Bilayered Systems. Philos. Mag. 95, 3208–3224. https://doi.org/10.1080/14786435.2015.1014443.

Cai, Z.X., Fu, Y.B., 2019. Effects of Pre-Stretch, Compressibility and Material Constitution on the Period-Doubling Secondary Bifurcation of a Film/Substrate Bilayer. Int. J. Non-Linear Mech. 115, 11–19. https://doi.org/10.1016/j.ijnonlinmec.2019.05.001.

Cao, Y.P., Hutchinson, J.W., 2012a. Wrinkling Phenomena in Neo-Hookean Film/Substrate Bilayers. ASME J. Appl. Mech. 79, 031019. https://doi.org/10.1115/1.4005960.

Cao, Y.P., Hutchinson, J.W., 2012b. From Wrinkles to Creases in Elastomers: The Instability and Imperfection-Sensitivity of Wrinkling. Proc. R. Soc. A 468, 94–115. https://doi.org/10.1098/rspa.2011.0384.

Cerda, E., Mahadevan, L., 2003. Geometry and Physics of Wrinkling. Phys. Rev. Lett. 90, 074302. https://doi.org/10.1103/PhysRevLett.90.074302.

Diab, M., Zhang, T., Zhao, R., Gao, H., Kim, K.-S., 2013. Ruga Mechanics of Creasing: From Instantaneous to Setback Creases. Proc. R. Soc. A 469, 20120753. https://doi.org/10.1098/rspa.2012.0753.

Fu, C., Cheng, Z., Wang, T., Xu, F., 2022. An Asymptotic Modeling and Resolution Framework for Morphology Evolutions of Multiple-Period Post-Buckling Modes in Bilayers. Math. Mech. Solids 27, 1397–1411. https://doi.org/10.1177/10812865221083046.

Fu, Y.B., Cai, Z.X., 2015. An Asymptotic Analysis of the Period-Doubling Secondary Bifurcation in a Film/Substrate Bilayer. SIAM J. Appl. Math. 75, 2381–2395. https://doi.org/10.1137/15M1027103.

Gao, Q., Zhong, W.X., Howson, W.P., 2004. A Precise Method for Solving Wave Propagation Problems in Layered Anisotropic Media. Wave Motion 40, 191–207. https://doi.org/10.1016/j.wavemoti.2003.09.002.

Guo, Y., Nie, G., 2024. Theoretical and Numerical Analysis of Period-Doubling Bifurcation in Sandwich Systems. Int. J. Solids Struct. 294, 112744. https://doi.org/10.1016/j.ijsolstr.2024.112744.

Holland, M.A., Li, B., Feng, X.Q., Kuhl, E., 2017. Instabilities of Soft Films on Compliant Substrates. J. Mech. Phys. Solids 98, 350–365. https://doi.org/10.1016/j.jmps.2016.09.012.

Li, B., Cao, Y.P., Feng, X.Q., Gao, H.J., 2012. Mechanics of Morphological Instabilities and Surface Wrinkling in Soft Materials: A Review. Soft Matter 8, 5728–5745. https://doi.org/10.1039/C2SM00011C.

Liu, J., Bertoldi, K., 2015. Bloch Wave Approach for the Analysis of Sequential Bifurcations in Bilayer Structures. Proc. R. Soc. A 471, 20150493. https://doi.org/10.1098/rspa.2015.0493.

Liu, Z., Liu, Y., 2026. A Brief Review on Recent Progress of Surface Instabilities in Film–Substrate Systems. Acta Mech. Solida Sin. 39, 433–454. https://doi.org/10.1007/s10338-026-00727-8.

Peng, H., Gao, Q., Wu, Z., Zhong, W.X., 2012. Symplectic Approaches for Solving Two-Point Boundary-Value Problems. J. Guid. Control Dyn. 35, 653–659. https://doi.org/10.2514/1.55795.

Shen, J., Fu, Y.B., Pirrera, A., Groh, R.M.J., 2024. Wrinkling of Differentially Growing Bilayers With Similar Film and Substrate Moduli. J. Mech. Phys. Solids 193, 105900. https://doi.org/10.1016/j.jmps.2024.105900.

Sui, J., Chen, J., Zhang, X., Nie, G., Zhang, T., 2019. Symplectic Analysis of Wrinkles in Elastic Layers With Graded Stiffnesses. ASME J. Appl. Mech. 86, 011008. https://doi.org/10.1115/1.4041620.

Sun, J.Y., Xia, S., Moon, M.W., Oh, K.H., Kim, K.S., 2012. Folding Wrinkles of a Thin Stiff Layer on a Soft Substrate. Proc. R. Soc. A 468, 932–953. https://doi.org/10.1098/rspa.2011.0567.

Wang, B., Li, P., Li, R., 2016. Symplectic Superposition Method for New Analytic Buckling Solutions of Rectangular Thin Plates. Int. J. Mech. Sci. 119, 432–441. https://doi.org/10.1016/j.ijmecsci.2016.11.006.

Xu, F., Potier-Ferry, M., Belouettar, S., Hu, H., 2015. Multiple Bifurcations in Wrinkling Analysis of Thin Films on Compliant Substrates. Int. J. Non-Linear Mech. 76, 203–222. https://doi.org/10.1016/j.ijnonlinmec.2014.12.006.

Xu, X., Ma, Y., Lim, C.W., Chu, H., 2006. Dynamic Buckling of Cylindrical Shells Subject to an Axial Impact in a Symplectic System. Int. J. Solids Struct. 43, 3905–3919. https://doi.org/10.1016/j.ijsolstr.2005.03.005.

Yao, W., Zhong, W., Lim, C.W., 2009. Symplectic Elasticity. World Scientific, Singapore. https://doi.org/10.1142/6656.

Zang, J., Zhao, X., Cao, Y.P., Hutchinson, J.W., 2012. Localized Ridge Wrinkling of Stiff Films on Compliant Substrates. J. Mech. Phys. Solids 60, 1265–1279. https://doi.org/10.1016/j.jmps.2012.03.009.

Zhang, H.W., Zhong, W.X., 2003. Hamiltonian Principle Based Stress Singularity Analysis Near Crack Corners of Multi-Material Junctions. Int. J. Solids Struct. 40, 493–510. https://doi.org/10.1016/S0020-7683(02)00585-1.

Zhang, T., 2017. Symplectic Analysis for Wrinkles: A Case Study of Layered Neo-Hookean Structures. ASME J. Appl. Mech. 84, 071002. https://doi.org/10.1115/1.4036613.

Zhang, T., 2019. Deriving a Lattice Model for Neo-Hookean Solids From Finite Element Methods. Extreme Mech. Lett. 26, 40–45. https://doi.org/10.1016/j.eml.2018.11.007.

[dataset] Zhang, T., 2026. Code and Data for Period Doubling and Quadrupling of Wrinkles. GitHub, version 1.0.0. https://github.com/tengzhang48/nonlinear-symplectic-wrinkle-bifurcations/tree/v1.0.0.

Zhao, R., Diab, M., Kim, K.-S., 2016. The Primary Bilayer Ruga-Phase Diagram II: Irreversibility in Ruga Evolution. ASME J. Appl. Mech. 83, 091004. https://doi.org/10.1115/1.4033722.

Zhao, R., Zhang, T., Diab, M., Gao, H., Kim, K.-S., 2015a. The Primary Bilayer Ruga-Phase Diagram I: Localizations in Ruga Evolution. Extreme Mech. Lett. 4, 76–82. https://doi.org/10.1016/j.eml.2015.04.006.

Zhao, Y., Cao, Y.P., Hong, W., Wadee, M.K., Feng, X.Q., 2015b. Towards a Quantitative Understanding of Period-Doubling Wrinkling Patterns Occurring in Film/Substrate Bilayer Systems. Proc. R. Soc. A 471, 20140695. https://doi.org/10.1098/rspa.2014.0695.

Zhong, W.X., 1995. A New Systematic Methodology for Theory of Elasticity. Dalian University of Technology Press, Dalian, China.

Zhong, W.X., Williams, F.W., 1993. Physical Interpretation of the Symplectic Orthogonality of the Eigensolutions of a Hamiltonian or Symplectic Matrix. Comput. Struct. 49, 749–750. https://doi.org/10.1016/0045-7949(93)90077-Q.

Zhuo, L., Zhang, Y., 2015. The Mode-Coupling of a Stiff Film/Compliant Substrate System in the Post-Buckling Range. Int. J. Solids Struct. 53, 28–37. https://doi.org/10.1016/j.ijsolstr.2014.10.028.